Theoretical concepts underlying ECL generation

I Svir, A Oleinick, O Klymenko, Christian Amatore

CHAPTER 5

Theoretical concepts underlying ECL generation

I. Svir,[a,c] A. Oleinick,[a] O.V. Klymenko,[a,b] and C. Amatore [a,d]

[a] CNRS UMR 8640 PASTEUR, Ecole Normale Superieure-PSL Research University, Departement de Chimie, Sorbonne Universites, 24 rue Lhomond, 75005, Paris, France

[b] Department of Chemical and Process Engineering, University of Surrey, Guildford, GU2 7XH, UK

[c] Design Automation Department, Kharkiv National University of Radioelectronics, Nauky Ave., 14, Kharkiv 61166, Ukraine

[d] State Key Laboratory of Physical Chemistry of Solid Surfaces, College of Chemistry and Chemical Engineering, Xiamen University, Xiamen, 361005, China

- Corresponding author: Dr Prof. Irina SVIR (irina.svir@ens.fr)

Abstract

The growing demand for analytical methods for the detection of biological analytes has stimulated a renewed interest in electrochemical reaction sequences producing electronically excited species prone to emit a photon upon its return to the ground state, a process called Electrogenerated Chemiluminescence (ECL). Both known types of ECL mechanisms, the so called *annihilation* and *co-reactant* ECL, are of importance in physical chemistry, but it is the fact that many luminophore/co-reactant pairs may include biological amines as co-reactants that has made ECL the method of choice for bioanalytical purposes owing to its high sensitivity and immunity to noise. In this chapter we present theoretical analyses and approaches for numerical simulation of typical ECL systems of both types that help reveal limiting factors controlling the intensity of ECL emission and ways to quantitatively optimise such systems to enhance their analytical efficiency.

5.1 Introduction

Reaction mechanisms leading to the formation from species generated at electrodes of electronically excited states S* able to undergo spontaneous radiative decay through the emission of a photon have a special place in electrochemistry. This family of processes called Electrogenerated Chemiluminescence, or Electrochemiluminescence (ECL) for short, has been the subject of continued attention for the last five decades.[1-6] Although originally the interest in these processes was rooted in physical chemistry and driven by the possibilities they offered to study highly energetic homogeneous electron transfer reactions (ET) and probing the Marcus inverted region (by invoking competition between ET leading to fundamental states and ET resulting in excited product states followed by radiative decay[5]) more recent research has been primarily focusing on applications of ECL, specifically for important bioanalytical purposes.

In comparison with classical techniques, ECL provides several significant analytical advantages. First, low background noise is a distinctive feature of ECL since no external light excitation source is required compared to other photoluminescent techniques.[5,6] This is particularly important to avoid undesired background emissions from biological analytes.[6-11] Second, the optical analytical signal is practically immune to electrical noise present in the excitation system (electrode potential) owing to the spatial segregation of the electrode and the light emission zone and the resulting and diffusional filtering between them. The first two features thus enable extremely low limits of detection of the order of pM concentrations. Third, ECL analyses are typically simpler in preparation and less time-consuming in comparison with other analytical methods of comparable sensitivity.

There are two main types of reaction mechanisms leading to ECL: *annihilation* ECL and *co-reactant* ECL. *Annihilation* ECL was the first to be discovered, and involves the formation of light-emitting excited state through ‘annihilation’ (rapid homogeneous electron transfer) between an oxidised and a reduced forms of the same luminophore generated at the surface of a working electrode from its ground state. Since both an oxidised and a reduced forms are required for the

formation of S*, both forms must be stable and formed through reversible heterogeneous ET reactions. Also, since both forms must be present in the solution to enable the generation of S* through highly exergonic homogeneous ET, they must themselves be generated simultaneously or almost simultaneously, which points to two electrochemical techniques enabling this situation: (i) the original approach involving rapid double-potential step excitation of a single working electrode between potentials sufficient for diffusion-controlled oxidation/reduction of the luminophore,[5] or (ii) under steady state through using a two- or three-electrode assembly continuously generating both the anion and the cation.[12] In the latter case the electrodes must be positioned in close proximity to each other or forced mass transport should be employed to ensure anions and cations encounter each other at as large concentrations as possible.

In *co-reactant* ECL generation, the luminophore, or its oxidised or reduced form, reacts with another species that has been reduced or oxidised, respectively, to form through a series of reactions an excited state that undergoes emissive decay.[5,6,11] A number of luminophore/co-reactant couples have been discovered (most generally a tertiary amine, and a metal complex luminophore), and co-reactant ECL was quickly adopted for the detection of minute quantities of analytes that modulate emitted light intensity through interference in the reaction mechanism.[9-11,13-17] In some circumstances, the analyte itself can play the role of co-reactant (e.g., amino acids, like many other biological amines), leading to analyses requiring few reagents.[15-17] The specificity and selectivity of detection may be ensured by coupling an ECL system with separation techniques such as HPLC or electrophoresis, including microfluidic-driven columns. Regarding the detection of large biomolecules (nucleic acids, proteins, etc.) the main research efforts are directed towards the development of ECL-analogues of ELISA-immunoassays. In these approaches, owing to the high cost of the luminophore moiety, the target molecule is selectively bound to the luminophore (or to a carrier, e.g. a nanoparticle, loaded with many luminophore molecules to increase the ECL emission intensity) through classical antigen-antibody interaction, with the whole assembly being suitably placed inside the diffusion layer of the oxidized organic co-reactant to allow an optimal reaction yield and magnitude of ECL response.[16,17]

Although many contributions on bio-analytical applications of ECL have effectively relied on calibration[13, 17] to optimise these techniques, the true reaction mechanisms involved and their potential in terms of limits of detection and conditions for optimal performance cannot be fully unravelled without their thorough theoretical understanding, quantitative characterisation and optimisation.

Regardless of the mechanism type and experimental technique, these reaction mechanisms involve sequences of extremely rapid bi-molecular reactions in solution. As a result, the electronically excited state S* is generated within extremely thin reaction zones, and its concentration is exceedingly small owing to its fast depletion via emissive deactivation. These specific features of ECL reaction mechanisms allow the electrochemical current and emission intensity to be calculated analytically in a limited number of special cases and under the assumption of infinitely fast second-order reaction kinetics. However, in the general case numerical simulations are required to model reactions involved together with mass transport modes and electrochemical activation techniques employed. Importantly, such numerical procedures face considerable challenges owing to the drastically different temporal and spatial scales involved.

Hereafter, we present illustrative examples involving both types of ECL reaction mechanisms to highlight these challenges and offer effective ways of overcoming them to enable accurate simulation of not only the electrochemical currents (e.g. the total flux of electroactive species at the electrode) but also of ECL intensity produced by vanishingly small, both in magnitude and in spatial extent, distribution of the electronically excited species. From the point of view of experimental setup, the examples feature (i) a two-electrode anode-cathode system in which anions and cations of the luminophore are generated simultaneously at the respective electrodes under diffusion-limited conditions, (ii) a single working electrode (planar or microdisk) operating under cyclic voltammetric conditions to generate the precursors of the excited state, as well as (iii) a system in which the luminophore is bound to nanoparticles (NPs) tethered to the surface of a working electrode so that the luminophore results immobilised at a specified location within the diffusion layer of the organic co-reactant.

5.2 Theory: mathematical modelling and computing

As mentioned in the Introduction, both types of reaction mechanisms leading to ECL are characterised by the presence of extremely exergonic bimolecular homogeneous reactions as well as fast first-order reactions such as emissive deactivation of the electronically excited state. This implies that the problem possesses multiple drastically different spatial scales (e.g., the diffusion layer of freely diffusing species vs. the width of a fast reaction zone) that must be resolved simultaneously and with considerable precision. In particular, a numerical simulation procedure must enable accurate solutions to be obtained (i) for the fluxes of electroactive species at the electrode surface for accurate computation of the electrochemical current and thus accurate transmission, in the numerical solution, of the electrochemical activation into the bulk of solution, and (ii) concentration distributions away of the electrode, particularly that of S*. Accurate determination of the latter is crucial for the evaluation of the intensity of ECL emission:

$$I_{ECL} = \phi_{ECL} k^{ECL} \iiint_V [S^*]\, dV \tag{5.1}$$

where ϕ_{ECL} is the overall quantum yield, k^{ECL} is the first-order rate constant of the emissive decay reaction, and V is the solution volume. Note that, although the integral is taken over the volume of the entire solution (or to the extent of the largest diffusion layer) the concentration of S* is zero throughout most of it.

It is clear that, to address both of the above challenges simultaneously, special numerical techniques must be employed. In particular, increasing the resolution of a numerical grid (e.g., in a finite difference or finite element method) in regions where concentration gradients are large or where concentration distributions experience large curvatures (i.e. where gradients change most rapidly) results in the minimisation of discretisation error and thus improves solutions obtained. One way of achieving higher localised grid density is through coordinate transformations.[18-20] This is

particularly effective when the locations where concentrations change most rapidly is known *a priori* as, for example, in the vicinity of the electrode surface. A number of such transformations have been employed for different electrode geometries amenable to 1D or 2D formulations of the relevant mass transport equations owing to symmetries. As concentration distributions in real physical space can be highly nonlinear even for species that do not participate in homogeneous reactions, which makes them difficult to represent on a finite uniform grid, a coordinate transformation that renders those distributions as linear as possible in the new space would generally be preferred owing to the reduced number of grid elements required for accurate representation of solution(s). This is even more important in the case of 2D simulations of electrochemical reactions at microelectrodes characterised by so called 'edge effects', i.e., indefinite increase of current density towards electrode edges (or electrode/insulator boundaries) under amperometric conditions.[4] Perhaps the most efficient way of constructing coordinate transformations that resolve the issue of flux discontinuity while leading to linear concentration distributions of species undergoing uncomplicated diffusion under steady state is the use of (quasi)*conformal mappings*.[18-20] Indeed, the application of conformal transforms allows mapping a two-dimensional domain in the physical space, where flux lines may be extremely curved or experience singularities, onto a region in which they become parallel and singularities are eliminated. This is also the reason why conformal mappings are of great interest since through effective linearization of concentration profiles they often lead to analytical solutions of steady state diffusion problems. Over the years, we have developed a number of numerical approaches based on efficient coordinate transformations including those derived by us for specific situations such as disk,[20-24] ring,[25] microband,[26,27] double microband[28-33] and double hemicylinder[34,35] assemblies and applied them to the simulation of ECL systems in a range of experimental situations.[18,22,23,36-39]

The second challenge, viz., achieving sufficiently accurate approximation of the emitter concentration profile in the solution bulk, is more difficult or even impossible to address a priori since the location of the zone of localisation of S* changes with time and/or electrochemical excitation applied at the working electrodes(s). Thus, adaptive grid refinement is required to track

the movement of the reaction zones of fast homogeneous reactions in order to dynamically enhance grid resolution in these areas without incurring a tough computational penalty through using extremely dense grids throughout the simulation space. There exist computational methods that are well suited for dynamical grid adaptation, such as the Finite Element Method, and there are a number of general purpose software implementing this capability (e.g., COMSOL Multiphysics[40]). Despite these implementations being relatively general, they are not intrinsically well suited to resolve both of the above challenges specific to electrochemical problems, and require detailed understanding of the system by the user to manually control the refinement of the computational mesh, especially to account for 'edge effects' at microelectrodes.[4,18,19] Nevertheless, software like COMSOL Multiphysics can be a powerful tool, particularly for non-standard geometries when the simulation is set up properly as demonstrated in Section 5.5.

We have developed a combined approach building on the advantages of both efficient coordinate transformations to deal with the complications due to diffusional mass transport and adaptive computational grids to track and resolve acute reaction fronts in solution (see Figure 5.1). This approach has been implemented in our general electrochemical software KISSA-1D[41-48] (for planar, (hemi)spherical or (hemi)cylindrical electrodes) and KISSA-2D[49] (for disk and band electrodes) capable of simulating reaction mechanisms of any complexity, including adsorption-desorption kinetics and reactions in the adsorbed state,[50,51] under a wide range of electrochemical techniques.

[**Figure 5.1** near here]

5.3 Theory of transient and steady-state ECL at dual hemi-cylinder electrode assemblies

Implementation of ECL reaction mechanisms at electrode arrays or assemblies of anodes and cathodes allows for steady state emission intensity to be achieved. In this section we provide a typical example of a theoretical study involving one such assembly consisting of two hemicylindrical electrodes of equal radius r_{hc} and length L separated by a gap of width g and

sustaining annihilation-type ECL in which the luminophore in its ground state A_g undergoes the following sequence of reactions to produce its cation, A^+, and anion, A^- radicals which upon highly exergonic ET produce an excited singlet state $^1A^*$ that returns to the ground state by emitting a photon γ_{ecl}:

$$A_g - e \rightarrow A^+ \qquad \text{(anode)} \qquad (5.2)$$

$$A_g + e \rightarrow A^- \qquad \text{(cathode)} \qquad (5.3)$$

$$A^+ + A^- \xrightarrow{k_{bi}} {}^1A^* + A_g \qquad \text{(fast electron transfer in solution)} \qquad (5.4)$$

$${}^1A^* \xrightarrow{k_f} \gamma_{ecl} + A_g \qquad \text{(fast deactivation in solution)} \qquad (5.5)$$

Scheme 1. Annihilation-type ECL mechanism

This is a classical reaction scheme, however, the electrode geometry, although seemingly trivial, is not easily amenable to numerical simulation using traditional numerical methods such as finite differences owing to the presence of curved boundaries. On the other hand, it has been recognized that, in comparison with double band electrodes, the protrusion of hemicylinders over the surface of the insulator enhances collection efficiencies when operated in the generator-collector mode,[34] which promises higher emission intensities if applied to ECL generation. Thus we wish to test this hypothesis and characterize the electrochemical currents and light intensities produced at double-hemicylinder electrodes through Scheme 1 versus those for a double-band system.

Under the assumption that the hemicylindrical electrodes are sufficiently long, the system can be considered in two spatial dimensions as shown in Figure 5.2a with the two semi-circles representing the surfaces of the two electrodes while the abscissa axis represents the insulator and the solution above it is assumed to be semi-infinite. The curved lines in the space corresponding to bulk solution represent flux lines connecting the surfaces of the two electrodes and equiconcentration lines of a freely diffusing species generated at one of the electrodes and depleted

at the other under steady state. Incidentally, these lines also represent the images of straight and mutually perpendicular coordinate lines in the transformed space (Figure 5.2b) obtained through the following conformal mapping developed by us previously:[34]

$$X = \frac{a\,e^{-\xi} - (a-b)\cos\eta + b\,e^{\xi}}{2(\cosh\xi - \cos\eta)} \tag{5.6}$$

$$Y = \frac{(a-b)\sin\eta}{2(\cosh\xi - \cos\eta)} \tag{5.7}$$

where $X = x/r_{hc}$ and $Y = y/r_{hc}$ are the normalized Cartesian coordinates, $a = \frac{1}{2}\left(2 + G - \sqrt{G^2 + 4G}\right)$, $b = \frac{1}{a}$, and $G = \frac{g}{r_{hc}}$. The inverse transformation from the (X, Y) space into the (ξ, η) space:[34]

$$\xi = \ln\left[\frac{\sqrt{\left[(X-b)(X-a)+Y^2\right]^2 + (a-b)^2 Y^2}}{(X-b)^2 + Y^2}\right] \tag{5.8}$$

$$\eta = \arctan\left[\frac{(a-b)Y}{(X-b)(X-a)+Y^2}\right] \tag{5.9}$$

The above transform (5.6)-(5.7) and its inverse (5.8)-(5.9) thus provide access to exact analytical solutions for concentrations of freely-diffusing species under steady state. In the case of transient conditions or when homogeneous reactions are present numerical solution of the relevant diffusion-reaction equations may still be required.

[**Figure 5.2** near here]

Considering reaction Scheme 1, transient electrochemical currents at the anode and cathode can be expressed in the conformal space as:

$$I_a(\tau) = -F\,D\,L\,c_0 \int_{\pi}^{2\pi} \left[\frac{\partial C^+}{\partial \xi} - \frac{\partial C^-}{\partial \xi}\right]\Bigg|_{\xi=\xi_1} d\eta \tag{5.10}$$

$$I_c(\tau) = F\,D\,L\,c_0 \int_{\pi}^{2\pi} \left[\frac{\partial C^+}{\partial \xi} - \frac{\partial C^-}{\partial \xi} \right]\Bigg|_{\xi=\xi_2} d\eta \qquad (5.11)$$

where $\tau = Dt / r_{hc}^2$ is the dimensionless time, D is the diffusion coefficient assumed to have the same value for all four species; $\xi_1 = \ln\left[(r_{hc} - a)/(b - r_{hc})\right] = -\xi_2$, F is the Faraday constant, L is the length of the electrodes (in the direction perpendicular to Figure 5.2a), and c_0 the initial concentration of species A_g. $C^+ = [\mathrm{A}^+]/c_0$ and $C^- = [\mathrm{A}^-]/c_0$ are the dimensionless concentrations of the cation- and anion-radicals respectively. It should be noted that the evaluation of the currents in the conformal space is drastically simplified since electrodes surfaces are transformed from semi-circles to merely straight vertical segments.

The transient ECL intensity, expressed in the units of photons/second, is computed in the conformal space by integrating the emitter concentration (see Figure 5.2c,d for typical transient distributions of $^1\mathrm{A}^*$ in the real and conformal spaces, respectively):

$$\Phi_{ecl}(\tau) = \varphi N_A \frac{d\, n_{\gamma ecl}}{dt} = \varphi N_A\, k_f\, L\, r_{hc}^2\, c_0 \int_{\xi_1}^{\xi_2} \int_{\pi}^{2\pi} \mathrm{C}^* \left| \frac{\partial(X, Y)}{\partial(\xi, \eta)} \right| d\eta\, d\xi \qquad (5.12)$$

where φ is the overall yield of $^1\mathrm{A}^*$, N_A is the Avogadro constant, $dn_{\gamma_{ecl}} / dt$ the photon flux, and $C^* = [^1\mathrm{A}^*]/c_0$ the dimensionless concentration of $^1\mathrm{A}^*$. The Jacobian of the conformal mapping (5.6)-(5.7), $\left| \frac{\partial(X, Y)}{\partial(\xi, \eta)} \right| = \frac{(a-b)^2}{4(\cosh\xi - \cos\eta)^2}$ describes the stretching of space upon the coordinate transformation. It is also a factor of the diffusion term in the diffusion-reaction equations describing the system at hand. Note that, despite an additional factor under the integral in (5.12) – the Jacobian – the integration is performed in a simple rectangular domain on a rectangular grid as opposed to a semi-infinite region with a curvilinear boundary in the original space.

As mentioned above, the application of the conformal mapping may yield analytical steady state solutions for concentrations and electrochemical currents. For the reaction mechanism at hand (Scheme 1) the situation is complicated by the fact that all the species participate in homogeneous

chemical reactions (5.4) and (5.5). However, considering the limiting case of infinitely fast annihilation reaction (5.4) its reaction front coincides with the interval $\xi = 0, \pi \le \eta \le 2\pi$ in the transformed space, where the concentrations of both the anion and cation vanish through reaction (5.4). Therefore, the steady state currents at the two electrodes are of the same magnitudes and have the value:

$$I_a = -FDLc_0 \frac{\pi}{\xi_1} = FDLc_0 \frac{\pi}{\xi_2} = I_c \tag{5.13}$$

and the dimensionless current defined as $f = I / FDLc_0$ is:

$$f^{ss} = \frac{\pi}{|\xi_1|} \tag{5.14}$$

while the dimensionless steady state ECL flux defined as $\Phi = \dfrac{\Phi_{ecl}}{N_A \varphi D L c_0}$ is:

$$\Phi^{ss} = \frac{\pi}{|\xi_1|} \tag{5.15}$$

Note that the steady-state current for the annihilation ECL mechanism in Scheme 1 is two times higher than that obtained for the same system operated in the generator-collector mode.[33] The same is true for any pair of identical electrodes when the diffusion coefficients of A^+ and A^- are the same as, e.g. in a double-band electrode system.[12,28,38] In this case, $|\xi_1| = \xi_2$ and the conditions $C^+ = 0$ and $C^- = 0$ apply at $\xi = 0$ while they apply respectively at ξ_2 and ξ_1 when the system operates in the generator-collector mode (i.e., when the ions are not annihilated in solution). Since both concentration distributions of A^+ and A^- are linear in the conformal space at steady state and their diffusion layers are half the width of those in the generator-collector mode, the resulting currents under ECL are double those for the generator-collector mode irrespective of the shape of the electrodes. This conclusion illustrates the power of analytical transforms that has led to a general conclusion that would be considerably more difficult to reach by considering the system in its physical space.

Steady state ECL intensity predicted by Equation (5.15) is proportional to the flux of the ions A^+ and A^- into the reaction zone of (5.4), as expected.[38] However, this solution should be considered as a limiting value that cannot be reached in a real experiment.[12,19,38] This occurs because the expression (5.15) assumes truly infinite equilibration time so that even the anions and cations diffusing away from each other may eventually react infinitely far from the electrode (i.e., the condition of zero fluxes towards the image of 'infinity' in the conformal space at point $\xi = 0$ and $\eta = 2\pi$ can apply only at mathematically rigorous steady state unachievable in reality).[12,19,34,38] Therefore, at large but finite times diffusional leaks of A^+ and A^- away from the electrodes would result in a deviation from the predicted limiting ECL intensity. In a realistic experiment, natural convection[45,46,53,54] would also facilitating the loss of the ions into the bulk of solution, although this situation would lead to a different limiting value of Φ^{ss}. To avoid these complications, we assume here pure diffusional transport and sufficiently high k_{bi}[4] so that the fraction of A^+ and A^- that may escape from their annihilation in reaction (5.4) remains vanishingly small.

The following numerical results are presented for a particular set of typical parameter values: $r_{hc} = g = 10\,\mu\text{m}$, $c_0 = 1\,\text{mM}$, $D = 10^{-5}\ \text{cm}^2\ \text{s}^{-1}$, $L = 0.2\ \text{cm}$, $k_{bi} = 10^9\,\text{M}^{-1}\text{s}^{-1}$, $k_f = 10^8\,\text{s}^{-1}$ and $\varphi = 10^{-2}$. Simulations were performed using the Alternating Direction Implicit (ADI) finite difference method on a grid of the size $N\xi \times N\eta \times N\tau = 100 \times 100 \times 10\,000$.[53]

Figure 5.3a,b shows transient variations of the current and ECL intensity reaching their respective steady states. It is clear that ECL intensity takes approximately ten times as long to reach its limiting values as the current, which corroborates the above conjecture.

It is of interest to compare the performance of the two-hemicylinder assembly with that of a double-band system when the surface areas of the electrodes are equal. To achieve this, the band width, w, should be related to the radius of the hemicylinder as $r_{hc} = w/\pi$ while keeping the other dimensions and parameters the same. Figure 5.3c demonstrates a comparison of steady state ECL fluxes at the two assemblies as a function of the gap size relative to the electrode size while

Figure 5.3d shows the time t^* to reach 80% of the respective steady state values for $w = 10\ \mu m$ and $r_{hc} \approx 3.183\ \mu m$. It is clear that at short separations (i.e., when g is comparable with r_{hc} or is less) the fact that hemicylindrical electrodes protrude over the insulator and effectively face each other with part of their surface area leads to drastically enhanced ECL intensities and reduces equilibration times, while at large separations the two ECL fluxes become indistinguishable. This mirrors the results reported previously for the generator-collector efficiencies obtained in these two systems.[33]

[**Figure 5.3** near here]

The use of a conformal mapping in the modelling of a two-hemicylinder microelectrode assembly sustaining annihilation ECL has allowed ready access to analytical solutions for species concentrations, current and ECL intensity at steady state. The same transformation also enabled efficient transient simulations to be performed owing to it being perfectly suited to tracking the relevant diffusion patterns. Moreover, conformal mappings help establish similarities (including equivalence relations) and differences between different electrodes and their assemblies at steady state and in transient conditions as has been done here for the case of double-band and two-hemicylinder assemblies.

5.4 Simulations of ECL in co-reactant systems

Co-reactant ECL systems generally follow considerably more complex reaction mechanisms than annihilation ECL. Herein we consider a system representing most of those used for bioanalytical purposes in physiological solutions. Such systems generally rely on tris(2,2′-bipyridine)ruthenium(II), $Ru(bpy)_3^{2+}$, as the luminophore and tripropylamine (TPrA), or another tertiary amine, as the co-reactant.[55] This system also happens to be the most studied both experimentally[11] and theoretically,[47,55,56] which enabled its thorough mechanistic and kinetic

characterisation. The $Ru(bpy)_3^{2+}$/TPrA is also mechanistically akin to other many other transition metals-based luminophores/co-reactants pairs currently being investigated, so the results of this study may be readily extended to such systems with the exception of specific thermodynamic and kinetic constants.

The reaction mechanism is summarised in Scheme 2, in which tripropylamine (TPrA) is used in a large excess in its neutral form (reaction (5.16)). It is oxidised irreversibly to yield a $TPrA^{\bullet+}$, a strong oxidant which, depending on the pH, may deprotonate irreversibly to produce a neutral radical ($TPrA^{\bullet}$) that is a strong reductant.[56] Upon reaching the electrode surface, $TPrA^{\bullet}$ can be oxidised into its corresponding iminium cation Im^+ that may undergo further follow-up reactions (Scheme 2). This process thus gives rise to a classical ECEC sequence in Eqns (5.17)-(5.20).[56,57] In the following, we do not consider the possibility that $TPrA^{\bullet}$ may be oxidized by $TPrA^{\bullet+}$ along a DISP1/DISP2 route[56] owing to the extremely short life-time of $TPrA^{\bullet+}$.[58,59]

Voltammetric studies evidenced[56] that owing to its large excess the amine oxidation wave is not visibly affected by the presence of $Ru(bpy)_3^{2+}$. This supports the conclusion that reactions (5.16)-(5.20) of Scheme 2 describe the main mechanistic sequence involving TPrA and its derivatives (the couple B/BH^+ represents a buffer). In other words, the effect of reactions of $TPrA^{\bullet+}$ and $TPrA^{\bullet}$ with Ru-based species on TPrA oxidation is practically negligible due to their small overall concentrations. On the other hand, these minor kinetic routes play a crucial role in the generation of ECL and are essential for understanding the luminophore reactivity.

Miao and Bard have demonstrated[56] that a transition metal complex luminophore, e.g., $Ru(bpy)_3^{2+}$, undergoes an exergonic ET with the electrogenerated $TPrA^{\bullet}$ thereby reducing $Ru(bpy)_3^{2+}$ into $Ru(bpy)_3^{+}$ (reaction (5.21)) This latter Ru(I) species is highly oxidizable,[56] so it reacts with $TPrA^{\bullet+}$ through an exergonic reaction that develops a sufficient Gibbs enthalpy for forming $Ru(bpy)_3^{2+}$*, the luminophore electronically excited state. $Ru(bpy)_3^{2+}$* then returns to the ground state species by emitting a visible photon, thereby closing the catalytic cycle powered by the TPrA oxidation (reactions (5.21)-(5.23) of Scheme 2).

A notable feature in the $Ru(bpy)_3^{2+}$/TPrA reaction scheme is that there are several routes leading to the generation of ruthenium excited state and hence emission of light. The first one, related to the amine oxidation and discussed above, appears as a first ECL wave at 0.88 V (see Figure 5.4). The second one is associated with the direct oxidation of $Ru(bpy)_3^{2+}$ at the electrode near 1.06 V and the following recombination of the oxidation product either with Ru^+ or $TPrA^\bullet$ (reactions (5.24)-(5.27) of Scheme 2). This is clearly marked in a typical set of simulated data in Figure 5.4 by the presence of two waves in the ECL signal, where each wave is linked with the redox potential of TPrA or $Ru(bpy)_3^{2+}$ as indicated in the figure.

In all pathways leading to photon emission Ru complexes behave akin to a catalyst and hence are not consumed. On the contrary reactions (5.19), (5.21), (5.27) and finally (5.20) convert TPrA and its oxidation derivative into inactive product, which necessitates a much larger co-reactant concentration (generally by a factor of several hundreds) vis-à-vis that of the luminophore.

$$TPrAH^+ + B \rightleftharpoons TPrA + BH^+, \tag{5.16}$$

$$TPrA - e \rightleftharpoons TPrA^{\bullet+}, \tag{5.17}$$

$$TPrA^{\bullet+} + B \rightleftharpoons TPrA^\bullet + BH^+, \tag{5.18}$$

$$TPrA^\bullet - e \rightleftharpoons Im^+ \tag{5.19}$$

$$Im^+ \xrightarrow{+H_2O} (CH_3)_2CO + DPrA, \tag{5.20}$$

$$TPrA^\bullet + Ru(bpy)_3^{2+} \rightleftharpoons Im^+ + Ru(bpy)_3^+, \tag{5.21}$$

$$TPrA^{\bullet+} + Ru(bpy)_3^+ \rightleftharpoons TPrA + Ru(bpy)_3^{2+*}, \tag{5.22}$$

$$Ru(bpy)_3^{2+*} \rightarrow Ru(bpy)_3^{2+} + h\nu, \tag{5.23}$$

$$Ru(bpy)_3^{2+} - e \rightleftharpoons Ru(bpy)_3^{3+}, \tag{5.24}$$

$$Ru(bpy)_3^+ - e \rightleftharpoons Ru(bpy)_3^{2+}, \tag{5.25}$$

$$Ru(bpy)_3^{3+} + Ru(bpy)_3^{+} \rightarrow Ru(bpy)_3^{2+} + Ru(bpy)_3^{2+*}, \quad (5.26)$$

$$TPrA^{\bullet} + Ru(bpy)_3^{3+} \rightleftharpoons Im^{+} + Ru(bpy)_3^{2+*}, \quad (5.27)$$

Scheme 2. ECL generation using $Ru(bpy)_3^{2+}$ as luminophore and TPrA as co-reactant

[**Figure 5.4** near here]

In Figure 5.4 the first ECL peak is considerably smaller than the second one, however, it is the first peak that represents a readout in most ECL-based analytical techniques. The analysis of the mechanism and simulated concentration profiles shows that the yield of the first catalytic pathway (and hence the magnitude of the first ECL peak) is conditioned by the presence of $TPrA^{\bullet}$, $TPrA^{\bullet+}$ and Ru^{+} in the same region of the solution. However as soon as Ru^{2+} becomes directly oxidizable at the electrode, Ru^{+} is partly annihilated by Ru^{3+}, but largely diffuses towards the bulk of the solution as clearly seen from the dynamic shift of the simulated concentration peak of the Ru^{2+*} (Figure 5.5) generated by the Ru^{3+}/Ru^{+} annihilation. This, in particular, explains the relatively small amplitude of the first ECL wave.

[**Figure 5.5** near here]

Retaining Ru^{+} closer to the electrode surface is thus expected to result in enhanced efficiency of the catalytic pathway (5.2)-(5.7) and intensity of the first ECL wave as it would be able to encounter higher concentrations of $TPrA^{\bullet}$ and $TPrA^{\bullet+}$. This can be achieved by decreasing the diffusion coefficients of all Ru-containing species[48] which, as illustrated in Figure 5.6 indeed leads to a substantial increase of the first wave intensity accompanied at the same time by a decrease in the second since the generation of Ru^{3+} at the electrode is diminished due to reduced diffusivity of Ru^{2+}.

This strategy can be implemented in practice through a suitable modification of the Ru-complex (e.g., by attaching a bulky or charged group) to reduce its diffusivity, through functionalization of nanoparticles or dendrimers with luminophore molecules or simply by immobilizing them at a given distance from the electrode via appropriate linker. Irrespectively of the selected approach the system can be optimized via a careful analysis of the luminophore and/or co-reactant transport to optimise placement of luminophore molecules within the diffusion field of co-reactant intermediates to increase the ECL signal.

[**Figure 5.6** near here]

All the simulations reported herein were performed using user-friendly KISSA©[41-45,47-49] software developed in our group that is capable of simulating complex reaction mechanisms such as that in Scheme 2 while accurately tracking and resolving fronts of reactions with rate constants up to the diffusion limit (i.e. 10^{10} $M^{-1}s^{-1}$) and over (which is useful for exploring various limiting cases).

5.5 Theoretical modelling and optimization of ECL from Ru^{2+} doped, immobilised silica nanoparticles

It has been established in Section 5.4 that reducing the diffusivity of the metal complexes in the co-reactant ECL reaction mechanism presented in Scheme 2 leads to increased ECL emission in the first wave due to enhanced catalytic activity of the metal complexes able to remain nearer the electrode surface. Ultimately, their mobility may be reduced to zero by employing one of the immobilisation techniques mentioned above. This is the approach that was undertaken by Paolucci group in the University of Bologna with $Ru(bpy)_3^{2+}$-doped core-shell silica nanoparticles (Figure 5.7a).[60-62] In this section we present a theoretical treatment of this system, where TPrA and the products of its oxidation diffuse freely while light is emitted from the core and/or in the shell of the NP[60,61] when reactive intermediates reach the immobilised $Ru(bpy)_3^{2+}$ complexes. This also means

that the $Ru(bpy)_3^{2+}$ species is not oxidizable or reducible at the electrode surface so that the reaction pathway (5.24)-(5.27) must be excluded. Apart from enhanced ECL signal, the advantages of this setup consist in achieving locally high concentrations of luminophore on a single label and protection of the luminophore from external factors.

While the reaction mechanism is known, there remains the challenge of finding an optimal position of Ru-laden NPs within the diffusion layer of TPrA (that can be controlled by adjusting the length of a suitable rigid linker) given particular experimental conditions. Optimization of the ECL intensity in such systems may depend on several other conditions like local pH or relation between certain rate constants, e.g. k_a and k_{ah} (Figure 5.7b). Indeed, reactions denoted by vertical double arrows in Figure 5.7b are protonation-deprotonation reactions, and their displacement is heavily dependent on the local pH of the solution. In order to maximize light emission the presence of a buffer at a certain concentration may be required. The delicate balance between the rates of these processes can have a drastic effect on the system's ECL performance. Therefore the influence of both of these factors for given NP linker length will be estimated theoretically.

[**Figure 5.7** near here]

Detailed simulation of the system at hand is a very challenging problem, primarily due to its multiscale nature (see Figure 5.8a). Indeed, a number of processes must be captured simultaneously in a single computation, i.e., (i) the whole diffusion layer of freely diffusing species (of the order of hundreds of micrometers), (ii) concentration variations near the electrode surface (from nanometric to micrometric scale), as well as (iii) reaction fronts caused by extremely fast kinetics inside the NP (nanometric scale). All of these different spatial scales can be accounted for in a single simulation in general purpose Finite Element software such as COMSOL Multiphysics,[40] however extreme care should be taken in the construction of the simulation mesh to ensure steep gradients and curvature of concentration profiles can be accurately represented. Such a simulation is necessarily very time-consuming because of a high number of nodes in the computational mesh (Figure 5.8a) as well as the number of species whose concentrations must be simulated. Therefore, although such

simulations may give accurate solutions for particular sets of parameters, they are poorly suited for the exploration of the whole parameter space and optimisation which require multiple model evaluations under different conditions (distances, concentrations, rate constants etc.), as well as for distinct systems employing, for instance, different amine (e.g. 2-(dibutylamino)ethanol) or luminophore (e.g., iridium or osmium complexes). Therefore, a less computationally demanding approach is required for such purposes. It has been established[63] that, unless the nanoparticle shell is unrealistically close to the electrode surface, computationally expensive 2D simulations can be replaced with fast 1D simulations centred at the nanoparticle centre (see Figure 5.8a) and limited to a few nanometres outside the nanoparticle shell. The correspondence between the two simulations for a particular configuration is illustrated in Figure 5.8b revealing small deviations while achieving a tremendous computational speed-up.

[**Figure 5.8** near here]

The results of a series of 1D simulations are summarised in Figure 5.9a depicting variations of the ECL intensity, I_{ECL}, with the distance z_{NP} from the centre of the core-shell nanoparticle to the electrode. Notably, this dependence is non-monotonic and exhibits a maximum at a distance $z_{\mathrm{NP}}^{\mathrm{max}}$ from the electrode that is dependent on $\sigma = k_{\mathrm{a}}/k_{\mathrm{ah}}$. Interestingly, it can also be demonstrated that $I_{\mathrm{ECL}} \approx \chi[\mathrm{TPrA}^{\bullet+}]_{\mathrm{soln}}$, where χ is a function of k_{ah}. Figure 5.9 shows that $\chi(k_{\mathrm{ah}})$ depends on k_{ah} through as sigmoidal function:

$$\chi(k_{\mathrm{ah}}) \approx \chi^{\infty}/[1 + (\Lambda/k_{\mathrm{ah}})^{\omega}] \tag{5.28}$$

where χ^{∞} is the value of χ for an infinite k_{ah} value, $\Lambda \approx 1.9 \times 10^{9}\mathrm{M}^{-1}\mathrm{s}^{-1}$ and $\omega \approx 0.5$. Thus, making use of an analytical approximation of the concentration $[\mathrm{TPrA}^{\bullet+}]_{\mathrm{soln}}$ as a function of distance under chronoamperometric conditions,[63] it can be obtained that for $z_{\mathrm{NP}} > z_{\mathrm{NP}}^{\mathrm{max}}$:

$$I_{\mathrm{ECL}}(z_{\mathrm{NP}}) \propto \frac{[\mathrm{Ru}]_0[\mathrm{TPrA}]^{\mathrm{bulk}}}{\sqrt{\pi k_{\mathrm{dep}} t}} \times \frac{\exp(-z_{\mathrm{NP}}\sqrt{k_{\mathrm{dep}}/D})}{[1+(\Lambda/k_{\mathrm{ah}})^{\omega}]} \tag{5.29}$$

where $k_{\mathrm{dep}} = k_{\mathrm{f}}[\mathrm{B}]$ is the pseudo-first order rate constant of deprotonation in (5.18).

The expression in (5.29) bears drastic resemblance to the independently obtained expression for the rate of generation of the excited state limit at $\xi \gg 1$ of the simplified one in Eqn (20), viz.:

$$v_{\mathrm{ECL}}(z_{\mathrm{NP}}) \propto \frac{[\mathrm{Ru}]_0[\mathrm{TPrA}]^{\mathrm{bulk}}}{\sqrt{\pi k_{\mathrm{dep}} t}} \times = \gamma_{\bullet+} k_{\mathrm{ah}} \exp(-z_{\mathrm{NP}}\sqrt{k_{\mathrm{dep}}/D}) \qquad (5.30)$$

where $\gamma_{\bullet+}$ is the partition coefficient of $[\mathrm{TPrA}^{\bullet+}]$ at the NP-solution interface. In agreement with usual experimental observations, (i) v_{ECL} is proportional to $[\mathrm{Ru}]_0[\mathrm{TPrA}]^{\mathrm{bulk}}$, (ii) obeys a Cottrell-like time dependence and (iii) decreases upon increasing k_{dep}, i.e., the buffered pH should not be too basic.

The similarity between Eqns (5.29) and (5.30) indicates that the lumped parameter $\gamma_{\bullet+}k_{\mathrm{ah}}$ in (5.30) varies as $1/[1 + (\Lambda/k_{\mathrm{ah}})^{\omega}]$ in the range $z_{\mathrm{NP}} > z_{\mathrm{NP}}^{\mathrm{max}}$. This is an essential result since it establishes that the variations of $\gamma_{\bullet+}$ with k_{ah} cannot be neglected when predicting the variations of I_{ECL} amplitude for $z_{\mathrm{NP}} > z_{\mathrm{NP}}^{\mathrm{max}}$. Note that this relationship establishes that $\gamma_{\bullet+}$ and $1/\{k_{\mathrm{ah}}[1 + (\Lambda/k_{\mathrm{ah}})^{\omega}]\}$ play equivalent roles. Hence, the critical effect of the partition coefficient of $\mathrm{TPrA}^{\bullet+}$ was implicitly taken care of in our simulations. This justifies that $\gamma_{\bullet+}$ can be set to unity in simulations to decrease the number of parameters.

[**Figure 5.9** near here]

Despite drastic simplifications made in the derivation of Eqn (5.30),[63] the simplified analytical formulation explains the critical roles played by (i) the relative concentrations of amine cation radical and its follow-up radical around the nanoparticle carriers, and (ii) by the buffer pH and concentration. In particular, this evidenced that the optimal pH range should not be too basic vs. the pKa of the amine cation radical. Thus this analysis provides qualitative insight into what changes in experimental conditions would enhance ECL emission. Further investigation of these insights using 2D and 1D numerical simulations of the tripropylamine (TPrA) / tris(2,2′-bipyridine)ruthenium(II) co-reactant system with the metal complexes loaded within the core of core-shell nanoparticles enabled systematic optimisation of ECL performance of this system. In particular, it has been determined that maximum ECL emission corresponds to an electrode-

nanoparticle distance, z_{NP}^{max}, at which $[TPrA^{\bullet+}]_{soln} \approx [TPrA^{\bullet}]_{soln}$, i.e., $z_{NP}^{max} \approx (\ln 2)\sqrt{D/k_{dep}}$, where k_{dep} is the deprotonation rate constant of the cation radical $TPrA^{\bullet+}$. Importantly, the value of k_{dep} can be finely tuned by adjusting the base buffer concentration, so as to match z_{NP}^{max} precisely to the size of the antigen-antibody tethers linking the luminophore-doped nanoparticles to the electrode.

5.6 Conclusions

Electrochemical reaction mechanisms leading to the emission of light continue to be of interest and offer new opportunities for applications[64-70]. The discovery of co-reactant ECL and subsequently of its utility in the detection of minute amounts of biological targets triggered a renaissance in applied ECL research and the ensuing analytical methods featuring impressive limits of detection. However, despite this being an active area of research, many contributions do not seek to fully characterise systems under scrutiny focusing instead on their trial-and-error characterisation (or, in other words, calibration) and optimisation. Such an approach may yield satisfactory results in applications, however, deep fundamental understanding of the reaction mechanisms involved as well as the peculiarities of system operation can arguably offer significantly more insight into feasible ways of debottlenecking the system and enhancing its efficiency (e.g., for analytical purposes) while potentially uncovering new research avenues. Therefore, in this chapter, we attempted to illustrate the utility of thorough mathematical modelling of ECL systems while highlighting the associated challenges, e.g. tough requirements on numerical simulations due to extremely narrow fronts of highly exergonic homogeneous electron transfers and miniscule concentrations of electronically excited emitter species.

We have demonstrated the power of conformal coordinate transformations to yield analytical solutions at steady state while simultaneously providing perfectly tailored computational grids under transient conditions. Such transformations help resolve highly curved flux and equiconcentration

lines, particularly in presence of edge effects, into straight lines, which (i) simplifies the construction of computational meshes and (ii) enhances convergence, as illustrated on the case of a two-hemicylinder electrode assembly sustaining annihilation ECL through continuous generation of anion- and cation- radicals of the luminophore.

As a priori coordinate transforms, including conformal mappings, cannot efficiently resolve moving fronts of fast homogeneous reactions away from the electrode surface, we have developed an adaptive simulation method implemented in general electrochemical simulation software, KISSA. Accurate simulations of not only electrochemical currents but also of the concentrations of all reacting species offer a means of systematic exploration of ECL reaction mechanisms and mass transport effects controlling the efficiency of light emission. This has been illustrated on a classical TPrA / $Ru(bpy)_3^{2+}$ co-reactant ECL system revealing parameters responsible for the amplitude of the analytical signal, which quantitatively confirmed that the latter can be improved by reducing the diffusivity of the metal luminophore complexes.

In line with these findings, the present trend consists in sequestrating the luminophore at high concentration inside nanoparticles. The aim of this is to increase the ECL intensity per target analyte while minimizing the required quantity of expensive luminophore by immobilising within the diffusion layer of the oxidized organic co-reactant in order to enhance analytical ECL responses. We have presented an approach for the optimisation of carrier core-shell nanoparticle positions relative to the electrode surface for maximum ECL intensity involving analytical approximations, demanding multiscale 2D simulations of the nanoparticle-electrode system, and verifiably accurate and extremely fast 1D simulations to enable quantitative computational optimisation of this system.

Finally, we note that although this work was based on available thermodynamic and kinetic parameters pertaining to the classical TPrA / $Ru(bpy)_3^{2+}$ co-reactant ECL system, its predictions are fully relevant to most ECL co-reactant systems[64] as long as they obey similar mechanistic features, while simply having different thermodynamic and kinetic constants.

Acknowledgments

Authors of this Chapter greatly thank all our colleagues and scientists around the World such as Prof. Al Bard and Dr. Steve Feldberg from USA, Profs. Erkang Wang and Guobao Xu from China, Prof. Neso Sojic and Prof. Fred Kanoufi from France, Prof. Janine Mauzeroll from Canada, Dr. Giovani Valenti, Prof. Francesco Paolucci, Mr. Enrico Daviddi from Italy, and many others who stimulated our big interest to this phenomenon and its important applications for medicine, ecology, chemistry, electronics, biotechnology and life science. We thanks CNRS (UMR 8640) for support as well PSL-ENS and Sorbonne University. CA acknowledges CNRS for his Emeritus DRCE position and Xiamen University for a Distinguished Professor position.

References

[1] K.S.V. Santhanam, A.J. Bard. *J. Am. Chem. Soc*., 1965, **87**, 139.

[2] S.W. Feldberg, *J. Am. Chem. Soc*., 1966, **88**, 390.

[3] L.R. Faulkner, A.J. Bard, *Techniques of Electrogenerated Chemiluminescence* in *Electroanalytical Chemistry*, ed. A.J. Bard, Marcel Dekker, New York, 1977, Vol. 10, pp. 1-95.

[4] A.J. Bard, L.R. Faulkner, *Electrochemical Methods: Fundamentals and Applications*, John Wiley & Sons, New York, 2nd ed., 2002.

[5] J. A. Bard, *Electrogenerated Chemiluminescence*, ed. A.J. Bard, Marcel Dekker, New York, 2004, chapter 1.

[6] R. Pyati, M.M. Richter, *Annu. Rep. Prog. Chem., Sect. C: Phys. Chem*., 2007, **103**, 12.

[7] N. Hao, K. Wang, *Anal. Bioanal. Chem*., 2016, **408**, 7035.

[8] S. Senthil Kumar, A.J. Bard, *Anal. Chem*. 2013, **85**, 292.

[9] N. Sardesai, S. Pan, J. Rusling, *Chem. Commun*. 2009, **33**, 4968.

[10] V. A. Zamolo, G. Valenti, E. Venturelli, O. Chaloin, M. Marcaccio, S. Boscolo, V. Castagnola, S. Sosa, F. Berti, G. Fontanive, M. Poli, A. Tubaro, A. Bianco, F. Paolucci, M. Prato, *ACS Nano*, 2012, **6**, 7989.

[11] W. Miao, *Chem. Rev*., 2008, **108 (7)**, 2506.

[12] J.E. Bartelt, M.R. Deakin, C. Amatore, R.M. Wightman. Anal. Chem., 60, 1988, 2167.

[13] A. J. Stewart, J. Hendry, L. Dennany, *Anal. Chem*. 2015, **87**, 11847.

[14] G. Valenti, E. Rampazzo, E. Biavardi, E. Villani, G. Fracasso, M. Marcaccio, F. Bertani, D. Ramarli, E. Dalcanale, F. Paolucci, L. Prodi, *Faraday Discuss*., 2015, **185**, 299.

[15] H. Li, A. C. Sedgwick, M. Li, R. A. R. Blackburn, S. D. Bull, S. Arbault, T. D. James, N. Sojic, *Chem. Commun*. 2016, **52**, 12845.

[16] Y. Zhuo, N. Liao, Y. Q. Chai, G. F. Gui, M. Zhao, J. Han, Y. Xiang, R. Yuan, *Anal. Chem*. 2014, **86**, 1053.

[17] S. Du, Z. Guo, B. Chen, Y. Sha, X. Jiang, X. Li, N. Gan, S. Wang, *Biosens. Bioelectron*., 2014, **53**, 135.

[18] A. Oleinick, O.V. Klymenko, I. Svir, C. Amatore, *Luminescence in Electrochemistry*, ed. F. Miomandre and P. Audebert, Springer, Switzerland, 2017, Chapter 7 "*Theoretical Insights in ECL*", pp. 215-256.

[19] C. Amatore, *Physical Electrochemistry: Principles, Methods and Applications*, ed. I. Rubinstein, M. Dekker, New York, 1995, Chapter 4.

[20] C.A. Amatore, B. Fosset, *J. Electroanal. Chem*., 1992, **328**, 21.

[21] O.V. Klymenko, R.G. Evans, C. Hardacre, I.B. Svir, R.G. Compton, *J. Electroanal. Chem*., 2004, **571**, 211.

[22] I.B. Svir, A.I. Oleinick, *J. Electroanal. Chem*., 2001, **499**, 30.

[23] I.B. Svir, A.I. Oleinick, A.V. Klimenko, *J. Electroanal. Chem*., 2001, **513**, 119.

[24] Oleinick, C. Amatore, I. Svir, *Electrochem. Commun*., 2004, **6**, 588.

[25] C. Amatore, A. Oleinick, I. Svir, *J. Electroanal. Chem*., 2004, **564**, 245.

[26] M.R. Deakin, R.M. Wightman, C.A. Amatore, *J. Electroanal. Chem*., 1986, **215**, 49.

[27] C. Amatore, B. Fosset, *Anal. Chem*., 1996, **68**, 4377.

[28] B. Fosset, C.A. Amatore, J.E. Bartelt, A.C. Michael, R.M. Wightman, *Anal. Chem*. 1991, **63**, 306.

[29] C.A. Amatore, B. Fosset, M.R. Deakin, R.M. Wightman, *J. Electroanal. Chem*., 1987, **225**, 33.

[30] C. Amatore, A. Oleinick, I. Svir, *Electrochem. Commun*., 2004, **6**, 1123.

[31] I.A. Arkoub, C. Amatore, C. Sella, L. Thouin, J.-S. Warkocz, *J. Phys. Chem. B*, 2001, **105**, 8694.

[32] C. Amatore, C. Sella, L. Thouin, *J. Phys. Chem. B*, 2002, **106**, 11565.

[33] I.B. Svir, A.I. Oleinick, R.G. Compton, *J. Electroanal. Chem*., 2003, **560**, 117.

[34] C. Amatore, A.I. Oleinick, I.B. Svir, *J. Electroanal. Chem*., 2003, **553**, 49.

[35] C.A. Amatore, M.R. Deakin, R.M. Wightman, *J. Electroanal. Chem*., 1986, **206**, 23.

[36] C. Amatore, C. Pébay, L. Servant, N. Sojic, S. Szunerits, L. Thouin, *ChemPhysChem*, 2006, **7**, 1322.

[37] A.V. Kukoba, A.I. Bykh, I.B. Svir, *Fresenius' J. Anal. Chem*., 2000, **368**, 439.

[38] C.A. Amatore, B. Fosset, K.M. Maness, R.M. Wightman, *Anal. Chem*., 1993, **65**, 2311.

[39] C. Amatore, A. Oleinick, O.V. Klymenko, L. Thouin, L. Servant, I. Svir, *ChemPhysChem*, 2007, **8**, 1664.

[40] COMSOL Multiphysics (Version 5.3a), COMSOL, Inc., Burlington, MA.

[41] C. Amatore, O.V. Klymenko, I. Svir, *Electrochem. Commun*., 2010, **12**, 1170.

[42] C. Amatore, O.V. Klymenko, I. Svir, *Electrochem. Commun*., 2010, **12**, 1165.

[43] O.V. Klymenko, A. Oleinick, I. Svir, C. Amatore, *Russ. J. Electrochem*., 2012, **48**, 593.

[44] O.V. Klymenko, I. Svir, C. Amatore, Electrochem. Commun., 2010, **12**, 1378.

[45] C. Amatore, O.V. Klymenko, I. Svir, *Anal. Chem*., 2012, **84**, 2792.

[46] C. Amatore, C. Pebay, L. Thouin, A. Wang. *Electrochem. Commun., 11*, **2009,** 1269.

[47] O.V. Klymenko, I. Svir, C. Amatore, *ChemPhysChem*, 2013, **14**, 2237.

[48] I. Svir, A. Oleinick, O.V. Klymenko, C. Amatore, *ChemElectroChem*, 2015, **2**, 811.

[49] See web sites: http://kissagroup.com; http://www.emergentinstruments.com/wp/products/kissa-1d-electrochemical-simulation-software/.

[50] O.V. Klymenko, I. Svir, A. Oleinick, C. Amatore, *ChemPhysChem*, 2012, **13**, 845.

[51] O.V. Klymenko, I. Svir, C. Amatore, *J. Electroanal. Chem*., 2013, **688**, 320.

[52] O.V. Klymenko, I. Svir, C. Amatore, *Mol. Phys*., 2014, **112**, 1273.

[53] C. Amatore, S. Szunerits, L. Thouin, J.S. Warkocz, *Electrochem. Commun*., 2000, **2**, 353.

[54] C. Amatore, S. Szunerits, L. Thouin, J. S. Warkocz, *J. Electroanal. Chem*., 2001, **500**, 62.

[55] C. Amatore, A. Oleinick, I. Svir, *Electrochem. Commun*., 2003, **5**, 989.

[56] W. Miao, J.-P. Choi, A.J. Bard, *J. Am. Chem. Soc*., 2002, **124**, 14478.

[57] C. Amatore, J.-M. Savéant, *J. Electroanal. Chem*., 1977, **85**, 27.

[58] C. Amatore, J.-M. Savéant, *J. Electroanal. Chem*., 1978, **86**, 227.

[59] C. Amatore, J.-M. Savéant, *J. Electroanal. Chem*., 1979, **102**, 21.

[60] G. Valenti, E. Rampazzo, S. Bonacchi, T. Khajvand, R. Juris, M. Montalti, M. Marcaccio, F. Paolucci, L. Prodi, *Chem. Commun*., 2012, **48**, 4187.

[61] K. Imai, G. Valenti, E. Villani, S. Rapino, E. Rampazzo, M. Marcaccio, L. Prodi, F. Paolucci, *J. Phys. Chem. C*, 2015, **119**, 26111.

[62] G. Valenti, E. Rampazzo, S. Bonacchi, L. Petrizza, M. Marcaccio, M. Montalti, L. Prodi, F. Paolucci, *J. Am. Chem. Soc*., 2016, **138**, 15935.

[63] E. Daviddi, A. Oleinick, I. Svir, G. Valenti, F. Paolucci, C. Amatore, *ChemElectroChem*, 2017, **4**, 1719.

[64] Y. Yuan, S. Han, L. Hu, S. Parveen, G. Xu, *Electrochim. Acta*, 2012, **82**, 484.

[65] A. S. Danis, K. P. Potts, S. C. Perry, J. Mauzeroll. *Anal. Chem*., 2018, **90**, 7377.

[66] S. Kesarkar, E. Rampazzo, A.Zanut, F. Palomba, M. Marcaccio, G. Valenti, L. Prodi, F. Paolucci. *Curr. Opin. Electrochem*., 2018, **7**, 130.

[67] M. M. Chen, Y. Wang, S. B. Cheng, W. Wen, X. Zhang, S. Wang, W. H. Huang. *Anal. Chem*., 2018, **90**, 5075.

[68] A. Fiorani, G. Valenti, M. Iurlo, M. Marcaccio, F. Paolucci. *Curr. Opin. Electrochem*. 2018, **8**, 31.

[69] G. Valenti, E. Rampazzo, S. Kesarkar, D. Genovese, A. Fiorani, A. Zanut, F. Palomba, M. Marcaccio, F. Paolucci, L. Prodi. *Coord. Chem. Rev*. 2018, **367**, 65.

[70] T. Kai , M. Zhou, S. Johnson, H.S. Ahn, A.J. Bard. *J. Am. Chem. Soc.*, 2018, **140**, 16178.

Figure Captions

Figure 5.1 Implementation of a dual numerical optimisation strategy: quasi-conformal mapping for disk geometry employed along with adaptive grid at a disk microelectrode for an EE reaction mechanism with infinitely fast comproportionation reaction. Note the enhanced grid density near the electrode as well as in the solution to track the propagating reaction front created by the comproportionation reaction.

Figure 5.2. Cross-section of the two-hemicylinder electrode assembly in (a) the real physical space (x, y) and (b) conformal space (ξ, η). Panels (c) and (d) show simulated isoconcentration curves for $^1A^*$ in the real and conformal spaces, respectively, at $t = 0.1\,s$ when steady state is not yet achieved. The highest concentration of emitters is observed around the plane of symmetry with the size of zone of non-negligible emission comparable to r_{hc}. See text for simulation parameters. Isoconcentration curves correspond to the values of $\log([^1A^*]/c_0)$: -6.17; -6.19; -6.2; -6.23; -6.26; -6.31; -6.36;-6.42;-6.5; -6.6; -6.71; -6.86; -7.06; -7.32; -7.72; -8.4; -9.87; -14.72; -29.63 (bottom to top).

Figure 5.3 Transient (a) current and (b) ECL intensity (solid curves) and their respective steady state limits (dash-dot lines). Variations of (c) steady state ECL intensity and (d) time t^* to reach 80% of steady state emission intensity for (1) double-band and (2) two-hemicylinder electrode assemblies. See text for simulation parameters.

Figure 5.4. Simulated current and ECL signal of TPrA/$Ru(bpy)_3^{2+}$ system obtained via cyclic voltammetry at scan rate v = 0.1 V/s with [$Ru(bpy)_3^{2+}$] = 1 mM, [TPrA] = 0.1 M (values correspond to experimental results obtained at pH = 8.5).[56] Simulations performed for a planar electrode using KISSA-1D (V.1.2).

Figure 5.5. Diffusional propagation of the Ru^{2+*} species (reaction front between Ru^{3+}/Ru^{+}) sustaining part of the second ECL wave intensity; the times elapsed from the beginning of a voltammetric scan are indicated for each curve; inset shows displacement towards the bulk of Ru^{2+*} concentration peak with time (squared distances). Conditions are the same as in Figure 5.4. Simulations performed for a planar electrode using KISSA-1D (V.1.2).

Figure 5.6. Simulated ECL intensity for a set of different diffusion coefficient of Ru-containing molecules: 5 x 10^{-6}, 5 x 10^{-7}, 10^{-7}, 5 x 10^{-8}, 10^{-8}, 10^{-9} cm^2/s and a constant one for TPrA. Other conditions are the same as in Figure 5.4.

Figure 5.7 a) Schematic representation of a $Ru(bpy)_3$-doped silica core nanoparticle (NP) equipped with a PEG shell with an indication of the typical NP dimensions; b) Stimulation of ECL mechanism inside the NP through TPrA oxidation (see text and reference 63).

Figure 5.8. (a) Schematic representation of the electrode-nanoparticle system with typical numerical mesh in COMSOL Multiphysics. (b) Time variations of ECL intensity as predicted by the 2D (red) or 1D (black) simulations when the nanoparticle centre is positioned at a distance $z_{\mathrm{NP}} =$ 50 nm from the electrode. NP dimensions: core radius $r_{\mathrm{core}} =$ 5 nm, shell radius $r_{\mathrm{NP}} =$ 9 nm.

Figure 5.9. (a) ECL intensity as a function of distance z_{NP} between nanoparticle centre and electrode surface computed using 1D-simulations for different values of the ratio $k_{\mathrm{a}}/k_{\mathrm{ah}}$ as indicated. All other thermodynamic and kinetic parameters values were equal to those reported in the text. (b) Variations of χ/χ^{∞} with k_{ah} for $k_{\mathrm{a}} =$ 10^{10} $\mathrm{M^{-1}s^{-1}}$ and all other thermodynamic and kinetic parameters as reported in the text. Data adapted from ref. [63].

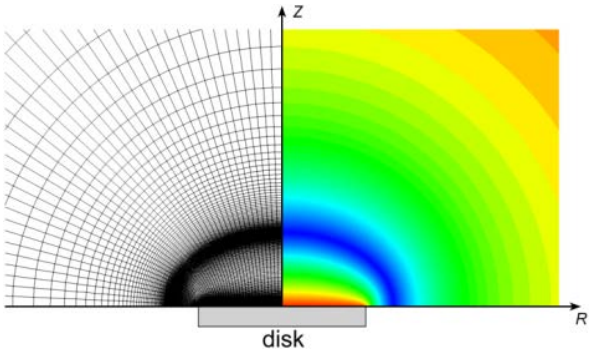

Figure 5.1

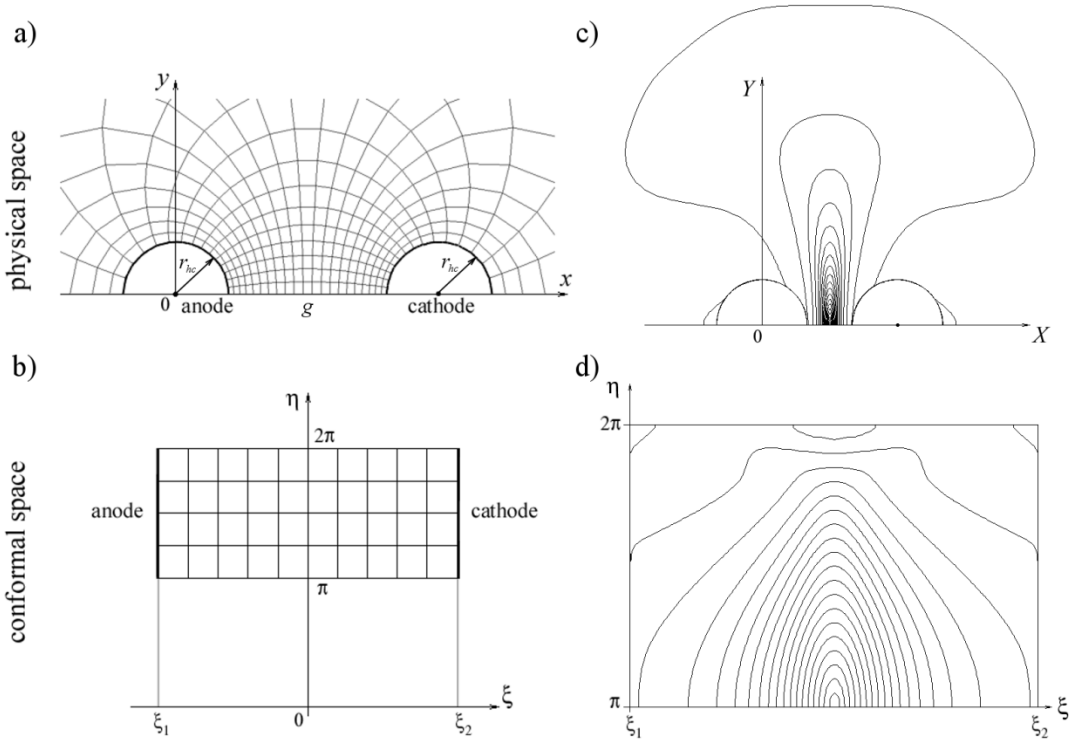

Figure 5.2

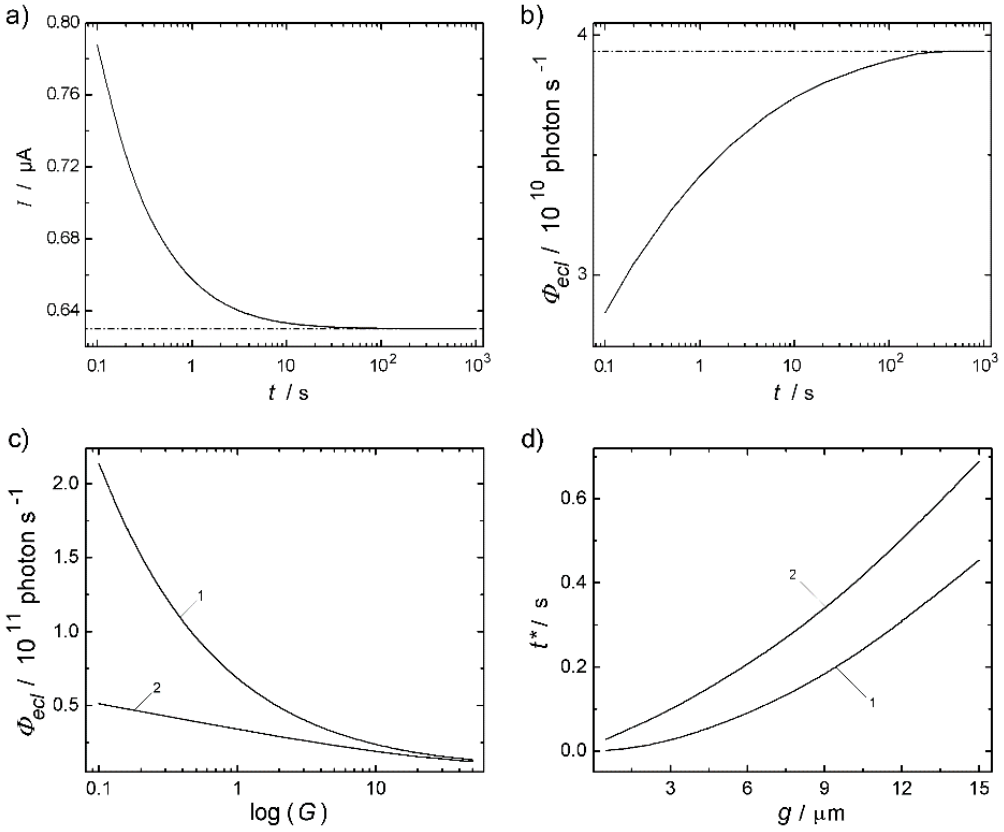

Figure 5.3

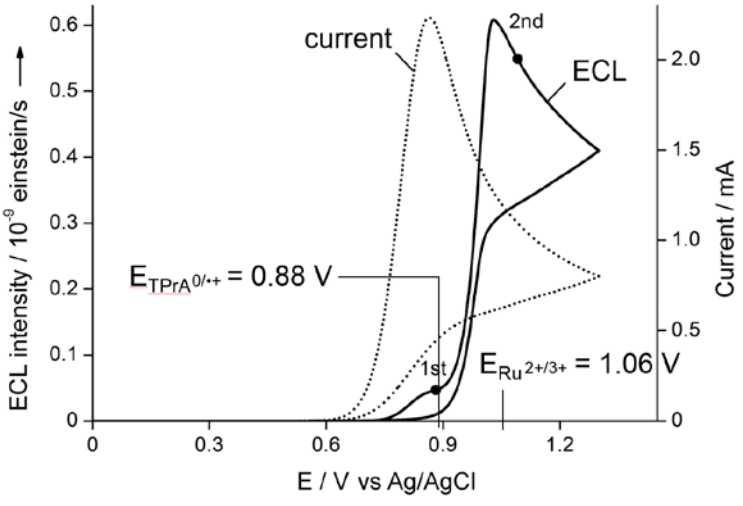

Figure 5.4

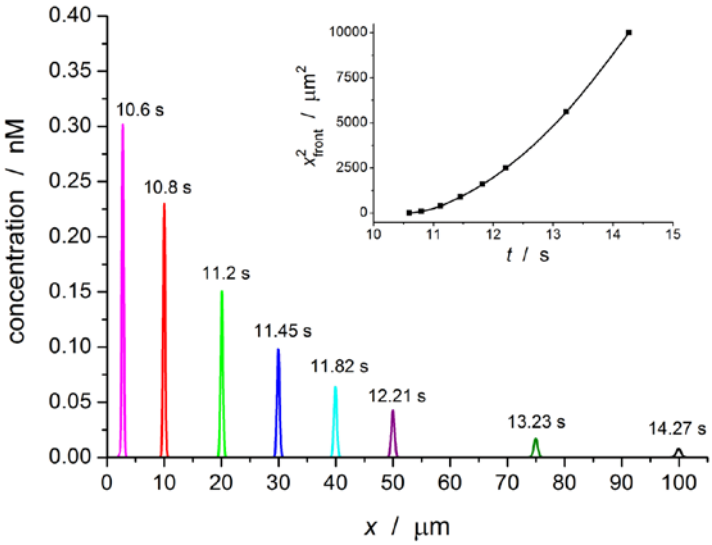

Figure 5.5

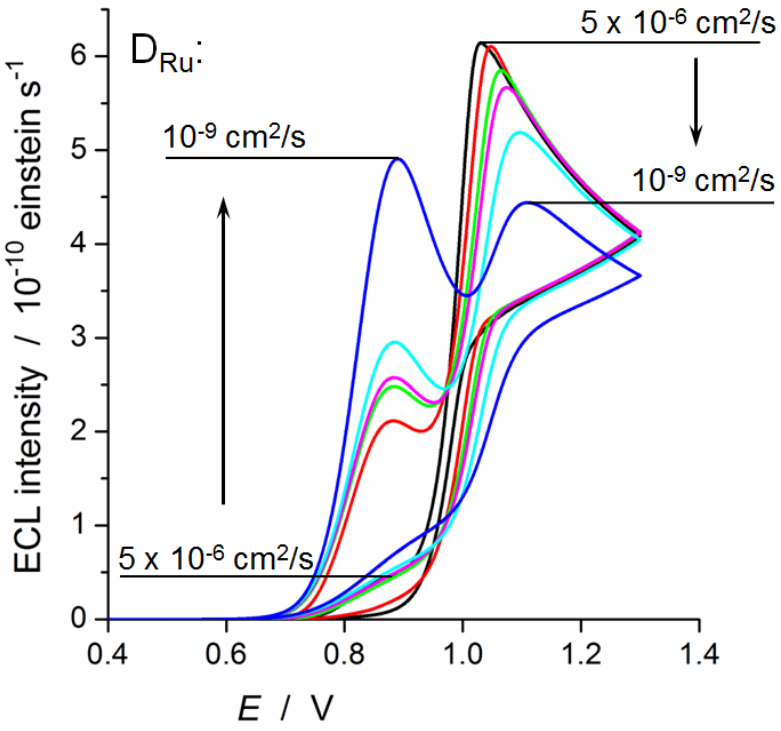

Figure 5.6

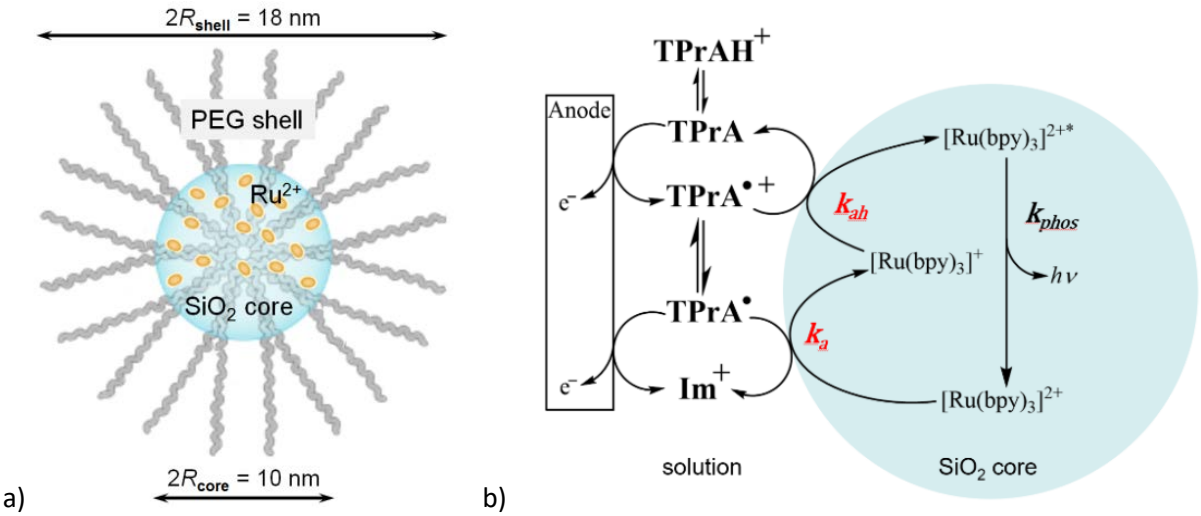

Figure 5.7

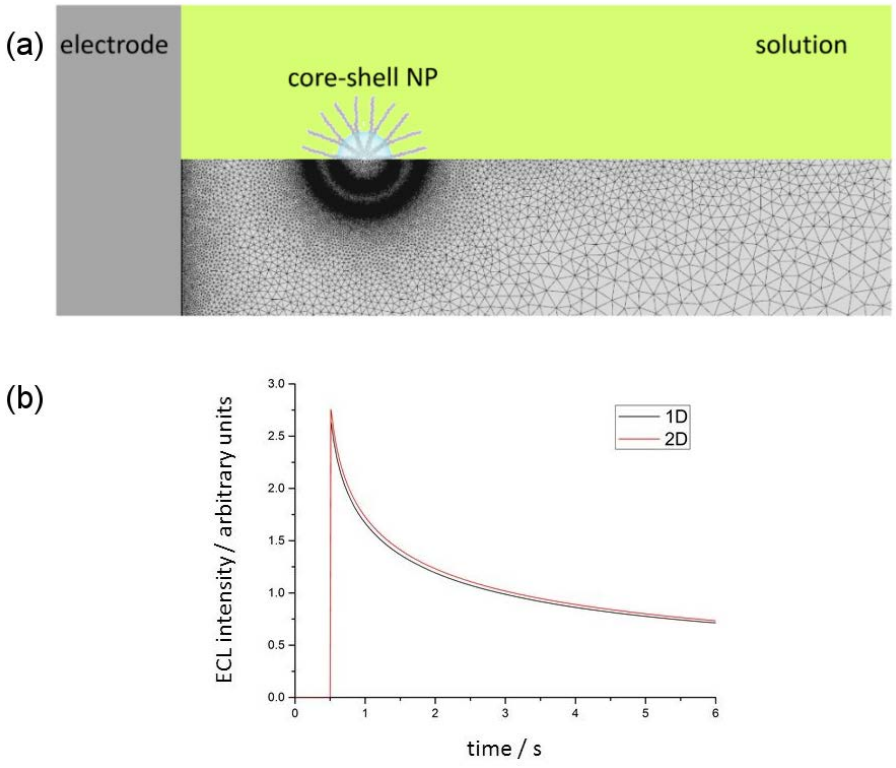

Figure 5.8

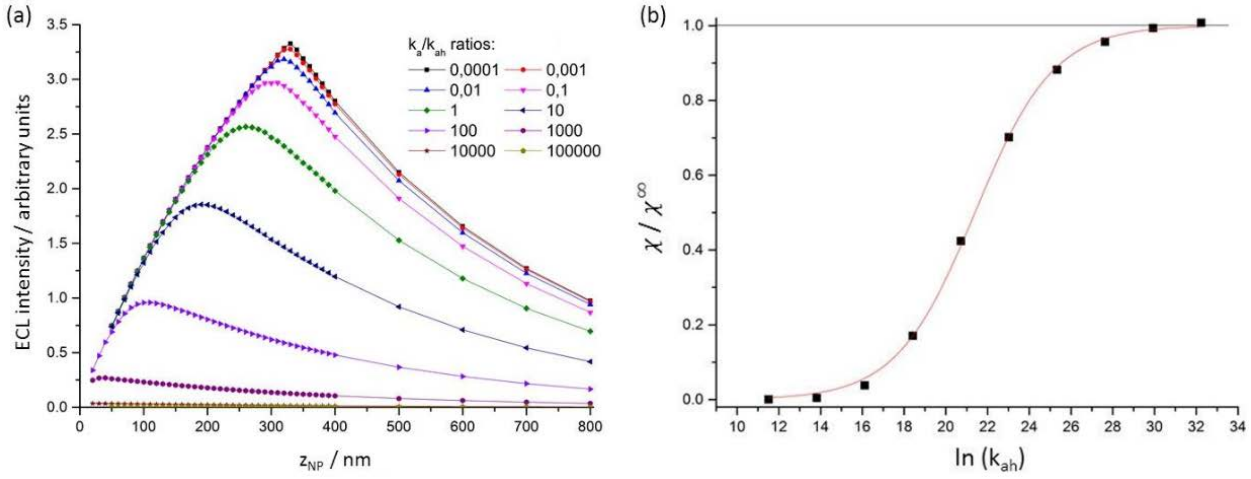
(a)
ECL intensity / arbitrary units
z_NP / nm
k_a/k_ah ratios:
0,0001
0,001
0,01
0,1
1
10
100
1000
10000
100000
(b)
χ / χ^∞
ln (k_ah)

Figure 5.9